

## Article

# Reactive Magnetron Sputtering for Y-Doped Barium Zirconate Electrolyte Deposition in a Complete Protonic Ceramic Fuel Cell

Victoire Lescure <sup>1,2</sup>, Mélanie François <sup>1</sup>, Maëlys Charleux <sup>1,2</sup>, Eric Aubry <sup>2</sup>, Lionel Combemale <sup>1</sup>, Pascal Briois <sup>2</sup>  
and Gilles Caboche <sup>1,\*</sup>

<sup>1</sup> Laboratoire Interdisciplinaire Carnot de Bourgogne, FCLAB, ICB-UMR6303, CNRS, Université de Bourgogne Franche-Comté, 9 Avenue Savary, BP47870, CEDEX, 21078 Dijon, France;

victoire.lescur@u-bourgogne.fr (V.L.); melanie.francois@u-bourgogne.fr (M.F.);  
maelys.charleux@u-bourgogne.fr (M.C.); lionel.combemale@u-bourgogne.fr (L.C.)

<sup>2</sup> Institut FEMTO-ST, FCLAB, UMR 6174, CNRS, Université de Bourgogne Franche-Comté, 15B, Avenue des Montboucons, 25030 Besançon, France; eric.aubry-01@utbm.fr (E.A.); pascal.briois@utbm.fr (P.B.)

\* Correspondence: gilles.caboche@u-bourgogne.fr; Tel.: +33-380396153

**Abstract:** Yttrium-doped barium zirconate is a commonly used electrolyte material for Protonic Ceramic Fuel Cells (PCFC) due to its high protonic conductivity and high chemical stability. However, it is also known for its poor sinterability and poor grain boundary conductivity. In this work, in response to these issues, reactive magnetron sputtering was strategically chosen as the electrolyte deposition technique. This method allows the creation of a 4  $\mu\text{m}$  thick electrolyte with a dense columnar microstructure. Notably, this technique is not widely utilized in PCFC fabrication. In this study, a complete cell is elaborated without exceeding a sintering temperature of 1350 °C. Tape casting is used for the anode, and spray coating is used for the cathode. The material of interest is yttrium-doped barium zirconate with the formula  $\text{BaZr}_{0.8}\text{Y}_{0.2}\text{O}_{3-\delta}$  (BZY). The anode consists of a NiO-BZY cermet, while the cathode is composed of BZY and  $\text{Ba}_{0.5}\text{Sr}_{0.5}\text{Co}_{0.8}\text{Fe}_{0.2}\text{O}_{3-\delta}$  (BSFC) in a 50:50 weight ratio. The electrochemical impedance spectroscopy analysis reveals a global polarization resistance of 0.3  $\Omega\text{ cm}^2$ , indicating highly efficient interfaces between electrolytes and electrodes.

**Keywords:** reactive magnetron sputtering; proton conducting ceramics; barium zirconate; tape casting; spray coating



**Citation:** Lescure, V.; François, M.; Charleux, M.; Aubry, E.; Combemale, L.; Briois, P.; Caboche, G. Reactive Magnetron Sputtering for Y-Doped Barium Zirconate Electrolyte Deposition in a Complete Protonic Ceramic Fuel Cell. *Crystals* **2024**, *14*, 475. <https://doi.org/10.3390/cryst14050475>

Academic Editor: Zhonghua Yao

Received: 29 March 2024

Revised: 7 May 2024

Accepted: 15 May 2024

Published: 18 May 2024



**Copyright:** © 2024 by the authors. Licensee MDPI, Basel, Switzerland. This article is an open access article distributed under the terms and conditions of the Creative Commons Attribution (CC BY) license (<https://creativecommons.org/licenses/by/4.0/>).

## 1. Introduction

Ceramics exhibit specific properties such as chemical resistance, high temperature resistance, electrocatalytic properties, and hardness and are used in a wide range of applications, particularly in the energy sector. Energy production stands as one of the global challenges of our century to reduce the emission of greenhouse gases and slow down global warming. The use of hydrogen in fuel cell systems is a promising alternative. Currently, Protonic Ceramic Fuel Cells (PCFC) are drawing more and more attention, as they are an excellent candidate due to their high protonic conductivity, above  $10^{-2}\text{ S cm}^{-1}$  at 600 °C [1–3], leading to noteworthy overall performances with a maximum power density higher than  $500\text{ mW cm}^{-2}$  at 650 °C [4–6]. In contrast to solid oxide fuel cells (SOFCs), where oxygen ions serve as the active species, PCFCs feature  $\text{H}^+$  ions as the active entities. This characteristic enables a reduction in operating temperatures within the range of 400–600 °C, owing to the higher mobility of  $\text{H}^+$  ions [7–9]. Lowering the operating temperature is crucial to extend the life expectancy of the cell. Also, thanks to the protonic conduction, water is formed at the cathode side, which prevents the fuel from being diluted [10,11].

$\text{BaCeO}_3$ -based oxides are currently the most studied electrolyte material for PCFCs [12–15]. It is generally reported that doped  $\text{BaCeO}_3$  exhibits the highest protonic conductivity among the perovskite-type materials [16,17]. In particular, Y-doped  $\text{BaCeO}_3$

(BCY) appears to be the most promising electrolyte candidate with a protonic conductivity equal to or superior to  $2 \times 10^{-2} \text{ S}\cdot\text{cm}^{-1}$  at  $600 \text{ }^\circ\text{C}$  [18–20]. However, BaCeO<sub>3</sub>-based perovskites show low stability in H<sub>2</sub>O and/or CO<sub>2</sub>-containing atmospheres, which limits their practical application [21–23]. Acceptor-doped BaZrO<sub>3</sub> is considered a good electrolyte material, especially with a substitution of 20% mol of yttrium [24–26]. In contrast to BaCeO<sub>3</sub>-based material, BaZr<sub>0.8</sub>Y<sub>0.2</sub>O<sub>3- $\delta$</sub>  (BZY20) presents excellent chemical stability [27–29]. However, it exhibits a lower total conductivity than BCY due to its high grain boundary resistance [30,31]. In addition, the highly refractive nature of BZY20 requires high sintering temperatures (1600–1700 °C) and long annealing times (>24 h) to achieve dense membranes with large grains and reach an appropriate total conductivity [15,32,33]. In this work, BZY20 was the chosen electrolyte material. To overcome its poor sinterability and poor grain boundary protonic conductivity, instead of adding sintering aids, the strategy was to employ physical vapor deposition in order to deposit a dense and columnar electrolyte layer to decrease the number of grain boundaries and thus increase the performance [6,34–36].

The anode, used as support for the complete cell, is a 400  $\mu\text{m}$  thick porous layer, enabling the fuel to be directed into the core of the cell [37]. It is made of a ceramic and metal composite called cermet, so the reaction can only occur in a specific zone named Triple Phase Boundary (TPB) [38]. The TPB is the point of contact between the three different phases: ceramic, metal, and gas present in the pores. Here, the ceramic is BZY20, and the metal is the widely used Ni obtained after NiO reduction [39]. Ni acts as a catalyst in the oxidation of hydrogen in addition to conducting electrons [40,41].

The cathode material is a composite consisting of a Mixed Ionic-Electronic Conductors (MIEC) and a protonic conductor in order to increase the number of TPBs [42,43]. Furthermore, the use of a composite cathode allows to reduce the Thermal Expansion Coefficient (TEC) mismatch existing between classical cathode and electrolyte material [44,45]. Among the different MIECs, Ba<sub>0.5</sub>Sr<sub>0.5</sub>Co<sub>0.8</sub>Fe<sub>0.2</sub>O<sub>3- $\delta$</sub>  (BSCF) was chosen due to its greater affinity with the electrolyte material [46–48].

To achieve good performance in a complete cell, it is necessary to control the microstructure of the electrolyte, especially the grain boundaries. In this work, multiple processes are used: tape casting, DC magnetron sputtering, and spray coating. Each has its own advantages. The anode bears all the mechanical properties of the cell; thus, it must be more solid and thicker than the rest. The method used to make it was tape casting, allowing a homogeneous layer [49,50]. Next, the electrolyte was deposited onto the anode by reactive magnetron sputtering, resulting in a thin, dense, and highly texturized layer [6,51]. The final component, the cathode, was then spray-coated. This method is convenient as it enables the electrode to be easily and simply placed on top of the electrolyte without any physical contact with it [52].

## 2. Materials and Methods

The complete cell was made by a succession of three different processes without exceeding 1350 °C: (1) tape-casting for the anode, which is used as the mechanical support of the cell, sintered at 1350 °C; (2) reactive magnetron sputtering for the electrolyte annealed at 1000 °C; and (3) spray coating for the cathode annealed at 800 °C. Figure 1 illustrates a schematic cell, highlighting the different shaping methods applied to each component's production.

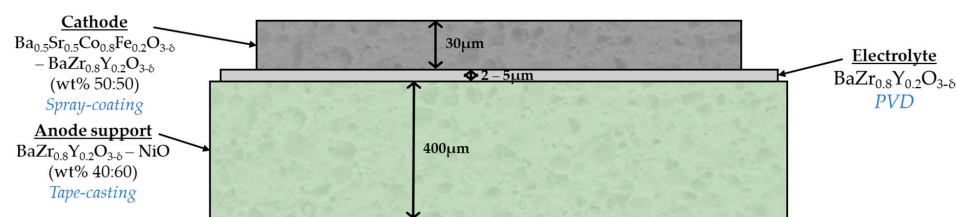


**Figure 1.** Schematic representation of the realized cell and the associated shaping process used.

### 2.1. Elaboration Process

The initial step consists of the preparation of the slurry. Ceramic powders BZY20 (provided by Cerpotech (Heimdal, Norway), lot #180120A-BZY20, with chemical purity > 99.0%) and NiO (provided by Fuel Cell materials (Colombus, OH, USA), lot #R5739, item #312010) were mixed together with a mixture of solvents, ethanol (Sigma Aldrich (St. Louis, MI, USA) #32205-M with a chemical purity of >99.8%) and Methyl Ethyl Ketone (Sigma Aldrich #78933 with chemical purity > 99.0%), along with a dispersant TEA (TriEthylAmine, Sigma Aldrich #90279 with a chemical purity of >99.0%). The components were mixed together in a Turbula-T2F device for 16 h with zirconia balls to achieve a homogeneous mixture. After that, PolyVinyl Butyral (PVB, Sigma-Aldrich #P110010) as binder and PolyethylEne Glycol (PEG, Sigma-Aldrich #P3015) and BenzylButyl Phthalate (BBP, Sigma-Aldrich #308501 with a chemical purity of 98%) as plasticizers are added. The slurry underwent an additional mixing period of 24 h. The detailed composition of the slurry is given in Table 1.

**Table 1.** Composition of the anode slurry (in g).

BZY	NiO	EtOH	MEK	TEA	PVB	PEG	BBP
24	36	14.4	14.4	3.15	11.1	2.25	2.25

The anode slurry is tape casted onto a glass plate using an automatic tape caster (Elcometer<sup>®</sup>, Manchester, UK) with a casting rate of 1 cm s<sup>-1</sup>. To prevent any air bubbles, the slip is de-aired beforehand. A homogeneous layer is obtained via a doctor blade, the gap of which from the glass plate is fixed between 1700 and 2000 µm. The thickness is determined by taking into consideration the drying and sintering shrinkage. After a drying time of minimum 24 h at room temperature, the cells are punch-cut to a diameter of 34 mm. The last step is the sintering at 1350 °C for 10 h with a heating and cooling rate of 3 °C min<sup>-1</sup>. A plateau at 360 °C for 1 h is applied to eliminate the organic compounds. The cells are covered with the electrolyte powder to prevent the Ba evaporation during the sintering [53–55].

Then, the BZY electrolyte layer was deposited by co-sputtering of Ba (purity 99.9%, Ø 50 mm × 3 mm) and Zr<sub>0.8</sub>Y<sub>0.2</sub> (purity 99.9%, Ø 50 mm × 6 mm) targets as described in previous work [56]. The reactor is a 90 L cylinder Alcatel 604 SCM (CIT Alcatel, Anancy, France) pumped down via a turbomolecular pump system that permitted a residual vacuum below 10<sup>-4</sup> Pa. The chamber is equipped with circular planar and water-cooled magnetron sputtering sources spaced 60 mm from the rotating substrate holder. The Ba- and Zr<sub>0.8</sub>Y<sub>0.2</sub>-targets are supplied with a pulsed DC (Direct Current) advanced energy dual generator authorizing the control of the discharge power. Argon (100 mL min<sup>-1</sup>) and oxygen (15 mL min<sup>-1</sup>) flow rates are controlled with Brooks flowmeters and the working pressure is kept at 1.2 Pa during deposition (working pressure measured using an MKS Baratron gauge, MKS Instruments, Andover, MA, USA). The anodes are placed on the rotating substrate holder at 40 mm from the substrate holder axis and are heated at 560 °C by radiative effect with a graphite electrical resistance heater placed behind the substrate holder. The powers applied to the two targets are optimized to obtain the required composition. The power applied on the Ba- target varies from 120 to 150 W and from 200 to 230 W for the Zr<sub>0.8</sub>Y<sub>0.2</sub>-target. The deposition speed in these conditions is 0.4 µm h<sup>-1</sup>. The half-cell was then annealed at 1000 °C for 2 h, with a heating rate of 3 °C min<sup>-1</sup> to ensure good densification and stress relaxation.

The cathode is deposited directly onto the electrolyte by spray coating via an airbrush. The slurry has to be more liquid than the slurry for tape casting. The liquid/solid ratio is 5 to 1, so the final slurry is slightly viscous. The composition of the slurry is given in Table 2. All the components are mixed by a Turbula for 24 h. Before the deposition, a 16 mm-circle template is tapped down onto the substrate to obtain a final cathode purposely smaller than the half-cell (anode/electrolyte). This prevents any short-circuits that could be caused by a contact between the anode and the cathode. The airbrush is held at 20 cm from the

substrate. Several deposition conditions were tested, as many parameters influence the final appearance of the cathode: the number of depositions, the duration of these sequences, the frequency, the drying time, etc. In the end, the selected method is 13 depositions of 5 s with a drying time of 2 min between each. This step is followed by an annealing treatment at 800 °C under air.

**Table 2.** Ink composition for the spray coating deposition (in g).

BZY	BSCF	Graphite	EtOH	TEA	PVB	PEG	BBP
5	5	0.4	50	0.106	1.2	1.2	0.75

## 2.2. Characterization

X-ray Diffraction (XRD) analysis was conducted on a Bruker D2 Phaser (Bruker Corporation, Billerica, MA, USA) coupled with linear detector Lynxeye\_XE\_T (Bruker Corporation, Billerica, MA, USA) using Cu K $\alpha$  radiation. The microstructure was investigated by scanning electron microscopy (SEM) on a Hitachi SU1510 coupled with a Bruker XFlash6110 (Bruker Corporation, Billerica, MA, USA) energy-dispersive X-ray (EDX) analyzer, on a Hitachi SU8230 (Hitachi, Tokyo, Japan) coupled with a Thermo-Scientific UltraDry EDS detector (Thermo Fisher Scientific, Waltham, MA, USA) and on a Thermo Fisher Scientific Phenom ProX desktop SEM (Thermo Fisher Scientific, Waltham, MA, USA). Weight losses during sintering were studied by thermogravimetric analysis (TGA) on a TA Instrument Q600 SDT (TA Instruments, New Castle, DE, USA) using the following procedure: ramp at 5 °C min<sup>-1</sup> to 360 °C, dwelling time of 1 h, ramp at 5 °C min<sup>-1</sup> to 1350 °C, dwelling time for 10 h. The roughness of the surface of the samples was determined by an Olympus DSX510 microscope (Olympus, Tokyo, Japan).

Electrochemical measurements were performed on a homemade test bench inspired by a Norecs ProboStat device (Norecs, Oslo, Norway). The reduction was carried out at 525 °C to decrease the kinetics of the chemical reaction. The anode side was fed by gas at 45.4 mL min<sup>-1</sup> with a pressure of 1.2 bar. Pure N<sub>2</sub> was sent during the increase in the temperature at 1.5 °C min<sup>-1</sup>. The cathode side was fed by dry air at 100 mL.min<sup>-1</sup> at 1.5 bar during the heating and the reduction. The quantity of H<sub>2</sub> was increased step by step by 5% until 50% for 2 h then by 10% for 90 min. The air flow was adjusted at 100 mL.min<sup>-1</sup> at a pressure of 1.7 bar. The final OCV was 0.78 V for 100% of wet H<sub>2</sub> at a pressure of 1.4 bar using a flow of 50 mL min<sup>-1</sup>. This OCV value is lower than expected due to gas leakages but was stable for some hours before dropping to 0 V due to the breaking of the sample during the increase in temperature from 525 to 550 °C. Electrochemical Impedance Spectroscopy (EIS) was carried out using a Metrohm PGSTAT302N (Metrohm, Herisau, Switzerland) from 10<sup>5</sup> Hz to 10<sup>-1</sup> Hz with an amplitude of 10 mV.

## 3. Results and Discussion

### 3.1. Characterization of the Anodic Substrate

A TGA was first performed to determine the behavior of the green anodic tape during the sintering process. The resulting thermogram, presented in Figure 2, consists of four distinct weight losses. The first one, noted A, occurs during the first ramp (between 20 and 300 °C) and accounts for 26.0%, corresponding to the degradation of binders, dispersants, and plasticizers and the evaporation of residual solvents. The second weight loss (1.6%), noted B, occurs between 300 and 955 °C and corresponds to the degas/dehydration of the bulk, which is known to happen between 600 and 700 °C in protonic conductors [57]. A third weight loss of 1.3%, noted C, is attributed to the decomposition of the BaCO<sub>3</sub> impurity initially present in the BZY powder (see X-ray diffractogram pattern of BZY powder on Figure A1 in Appendix A). And, finally, from 1300 °C until the end of the thermal treatment meaning after a dwell of 10 h at 1350 °C, the vaporization of BaO is visible represented by a weight loss of 1.5%, noted D.

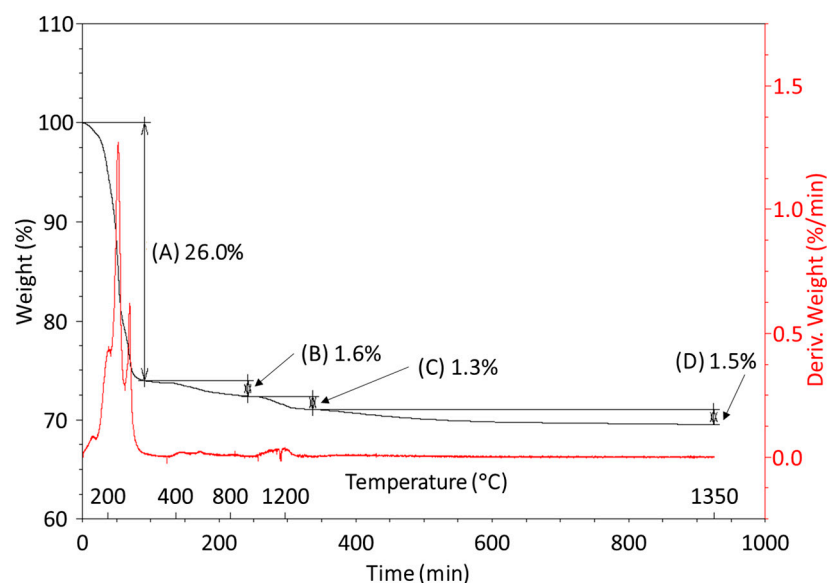


**Figure 2.** TGA of BZY-NiO anode material at 1350 °C for 10 h.

Based on these results, elemental analyses were conducted to observe any changes in BZY composition during the sintering process. The content of each element, as well as the theoretical content, is presented in Table 3. For comparison, a sample covered by BZY sacrificial powder and sintered under the same conditions was also studied. The composition of the anode after sintering without sacrificial powder is  $\text{Ba}_{0.89}\text{Zr}_{0.78}\text{Y}_{0.21}\text{O}_{3-\delta}$  with a ratio of A site/B site equals to 0.89 instead of 1. This result is consistent with the TGA study and confirms BaO vaporization at high temperatures. To prevent BaO vaporization during barium cerate and zirconate sintering, a solution is to use sacrificial powder [58,59]. As shown in Table 3, the ratio of A site/B site remains 1 after the sintering treatment using this strategy.

**Table 3.** EDX elemental analyses of the anode surface after sintering with and without sacrificial powder.

	Ba (A Site) at%	Zr (B Site) at%	Y (B Site) at%	Ratio (A Site)/(B Site)
Theoretical values	1.00	0.80	0.20	1
Without BZY sacrificial powder	$0.89 \pm 0.08$	$0.79 \pm 0.07$	$0.21 \pm 0.07$	0.89
With BZY sacrificial powder	$1.00 \pm 0.05$	$0.89 \pm 0.02$	$0.11 \pm 0.02$	1

X-ray diffraction patterns of the surface of the BZY-NiO anode after the sintering at 1350 °C for 10 h with and without sacrificial powder are presented in Figure 3. When sacrificial powder is used, the diffractogram consists of three different phases: perovskite structure with  $\text{BaZr}_{0.9}\text{Y}_{0.1}\text{O}_{2.95}$  composition (ICCD file N°00-064-0183, with lattice parameter of 4.212(3) Å calculated by Bragg's law), NiO (ICCD file N°00-047-1049) and  $\text{Y}_2\text{BaNiO}_5$  (ICDD file N°00-047-0090). Such  $\text{Y}_2\text{BaNiO}_5$  phase was also reported by other authors when an excess of BZY compared to NiO is employed during sintering [29,60,61]. In addition, Tong et al. and Liu et al. also reported that  $\text{Y}_2\text{BaNiO}_5$  promotes grain growth of BZY and leads to the appearance of electronic conductivity, which is detrimental to electrolyte application but beneficial to anode application [29,61].

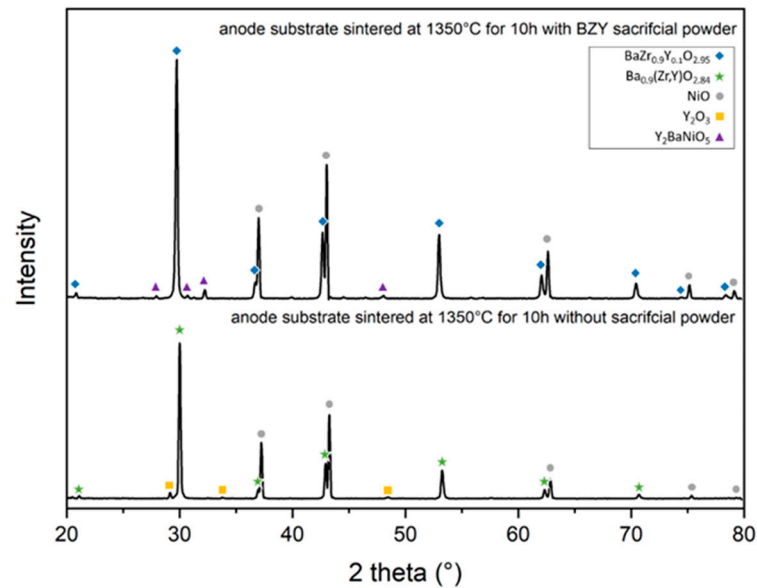


**Figure 3.** XRD patterns of the surface of the BZY anode after sintering at 1350 °C for 10 h. On the top: with BZY sacrificial powder; on the bottom: without any sacrificial powder.

Without any sacrificial powder, the perovskite structure proves once again the barium deficiency as it was identified with  $\text{Ba}_{0.9}(\text{Zr},\text{Y})\text{O}_{2.84}$  (ICCD file N°04-020-2236, with lattice parameter of 4.209(7) Å). NiO and  $\text{Y}_2\text{O}_3$  were also detected. This result provides clear evidence that under the sintering conditions, the samples decompose to form yttria doped zirconia (Equation (1) [62]) or yttria (Equation (2) [63,64]) and volatile barium species, BaO or  $\text{BaCO}_3$ , like as observed in other studies [62–67].

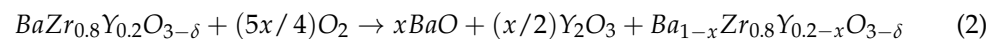
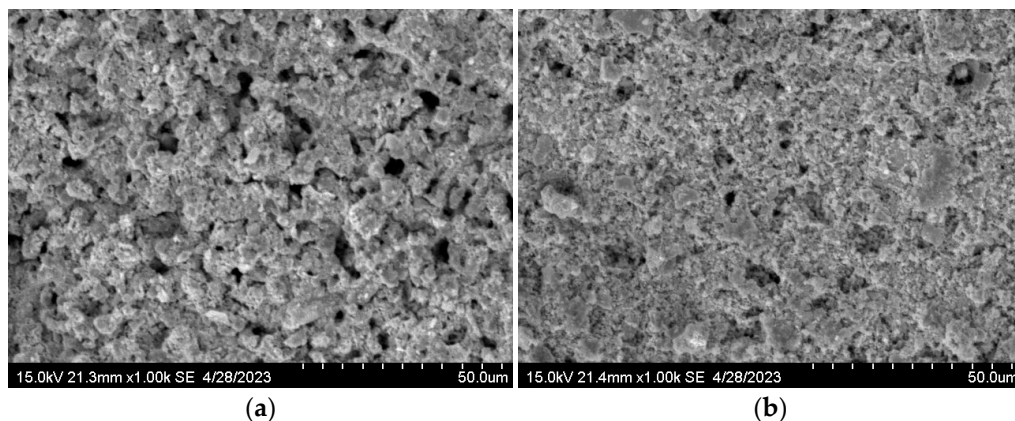
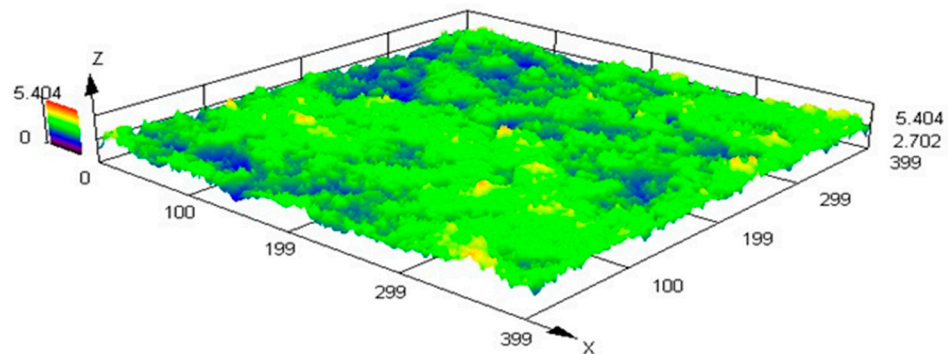


Figure 4 shows SEM micrographs of the BZY-NiO anode substrate after sintering at 1350 °C for 10 h in air without any sacrificial powder and after sintering with BZY sacrificial powder. Samples sintered with sacrificial powder exhibit a denser microstructure with an average porosity diameter of  $1.4 \pm 1.3 \mu\text{m}$ , determined using ImageJ software v. 1.54, while anode sintered without sacrificial powder shows an average porosity diameter of  $4.3 \pm 2.4 \mu\text{m}$ . Such micrometric porosity might lead to detrimental pinhole defects in the electrolyte layer due to shading effects during DC sputtering [68].



**Figure 4.** SEM micrographs of the BZY-NiO substrate surface, after annealing at 1350 °C for 10 h in air. (a): without any sacrificial powder. (b): with sacrificial powder.

To define the size and depth of the observed defects, 3D microscopy analyses were then conducted on the anode surface. Figure 5 shows the result obtained on a  $400 \times 400 \mu\text{m}$  square. The top value reaches  $1.3 \mu\text{m}$  and the lower value is near  $-1.4 \mu\text{m}$ . These values were obtained after calculating the mean top values and the mean lowest values of 10 different areas on the cell. So, to prevent any contact between the anodic and cathodic parts of the final cells, the electrolyte has to reach a minimum thickness equal to  $2.7 \mu\text{m}$ .



**Figure 5.** Three-dimensional microscopy of the anode substrate (scale in  $\mu\text{m}$ ).

### 3.2. Study of Thin Electrolyte Layer Deposition by PVD

By considering the previous observations, the electrolyte layer was then directly deposited on the anodic support by reactive magnetron sputtering. The aim was to realize a dense layer with a thickness superior to  $2.7 \mu\text{m}$ . Previous work [51] proved that using one single ceramic target to deposit ceramic electrolyte did not work, hence the use of a pure Ba metallic target and a  $\text{Zr}_{0.8}\text{Y}_{0.2}$  metallic target. Therefore, tests had to be made to adjust the composition of the thin film. The power applied to each target has a direct effect on the composition. Figure 6 shows how the stoichiometry varies as a function of the ratio of the powers applied to the targets. When the  $P_{\text{Ba}}/P_{\text{Zr}_{0.8}\text{Y}_{0.2}}$  ratio increases, the Ba-content, measured by EDX, decreases. A total of 140 W on the Ba target and 220 W applied on the  $\text{Zr}_{0.8}\text{Y}_{0.2}$  target was the closest to obtaining the convenient stoichiometry with a Ba/Zr + Y ratio close to 1.

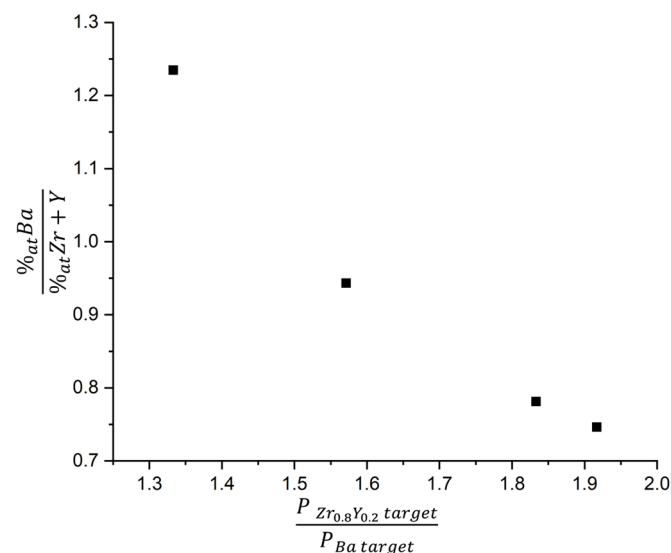


**Figure 6.** Variation of the atomic A site/B site ratio as a function of the applied power ratio on the targets during PVD deposition.

X-ray Diffraction is realized on the electrolyte to determine the final structures. Figure 7 shows the diffraction patterns of the deposited electrolyte before and after the annealing treatment in comparison with the theoretical XRD pattern of BZY obtained via CaRine

Crytallography software (v. 3.1). The pattern of the electrolyte before annealing treatment presents two BZY structures with cubic perovskite structure (space group Pm-3 m); one corresponds to the anodic substrate, and the second is assigned to the electrolyte. NiO, with its bunsenite structure, is also detected due to its presence in the anodic part. Concerning the BZY structure detected in the anodic substrate, a slight depletion of Ba is observed as these particular samples were not sintered under a bed of sacrificial powder. In the electrolyte coating, the BZY structure is clearly oriented following two main directions: [h00] (visible on [100] at 21° and [200] at 43°) and [211] visible at 53°. Also, a shift in the peaks of the electrolyte to the lower angles (highlighted with the purple dotted line in Figure 7 at 30°) is observed compared to the peaks of the pure BZY powder. This shift is due to the reductive atmosphere employed during the deposition, which creates oxygen vacancies and/or stresses in the coating. The formation of oxygen vacancies gives rise to lattice expansion with the loss of negatively charged oxygen, weakening the extent of ionic bonding. As a result, the XRD pattern is shifted towards the lower angles. These observations allow us to choose  $\text{Ba}(\text{Y,Zr})\text{O}_{2.6}$  (ICDD 04-021-8250) as the main phase of the electrolyte layer. To ensure good electrolyte layer densification and to compensate for an excess of oxygen vacancies, the half-cell was annealed for 2 h at 1000 °C. The thermal treatment has no impact on the anodic substrate. However, it has an effect on the electrolyte structure. In fact, the preferential growth-oriented [211] disappears, and only one preferential direction remains, following the [h00] plans. This reorientation is attributed to stress relaxation [69,70]. Also, the thermal treatment was realized under air, so the oxygen content increased within the structure. This explains the change to  $\text{Ba}(\text{Y,Zr})\text{O}_{2.95}$  structure (ICDD 04-011-7315) for the electrolyte.

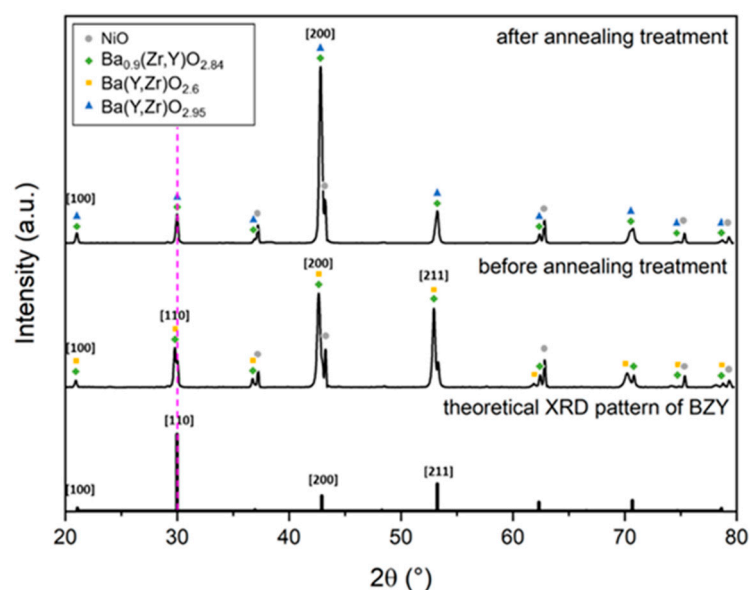


**Figure 7.** XRD patterns obtained after PVD deposition. On top: after the additional heat treatment at 1000 °C under air. In the middle: before the annealing treatment. At the bottom: a theoretical XRD pattern of the raw BZY powder. A shift in the peaks of the electrolyte to the lower angles is highlighted with the purple dotted line.

To ensure a perfect seal between the anodic and cathodic components, the electrolyte layer has to be as dense as possible and have a minimum thickness of 2.7  $\mu\text{m}$ . Figure 8 presents SEM observations on half cells, proving that these specifications are reached. The cross-section (Figure 8a) demonstrates the perfect adhesion between the anodic substrate and the electrolyte layers and shows a homogeneous thickness for this last. The deposited electrolyte has a columnar microstructure, as supposed after XRD studies and as observed in different publications [71,72]. It is a great advantage for the PCFC system because this morphology allows protons to traverse the electrolyte with little to no grain boundaries

to cross; this could improve the protonic conductivity performances, as proven by Bae et al. [6]. Figure 8b shows the impact of the thermal treatment at 1000 °C. The columnar structure is conserved, and a straightening of the columns is observed, agreeing well with the disappearance of the [211] direction seen on the XRD pattern. This could be explained by the mechanical relaxation during the annealing treatment. Finally, SEM pictures permit us to evaluate the electrolyte thickness ( $t$ ), which is close to 4  $\mu\text{m}$ , meaning bigger than 2.7  $\mu\text{m}$ , and to confirm the absence of porosities on the electrolyte surface (Figure 8c). The surface indeed appears flat without any trace of the underlying anode.

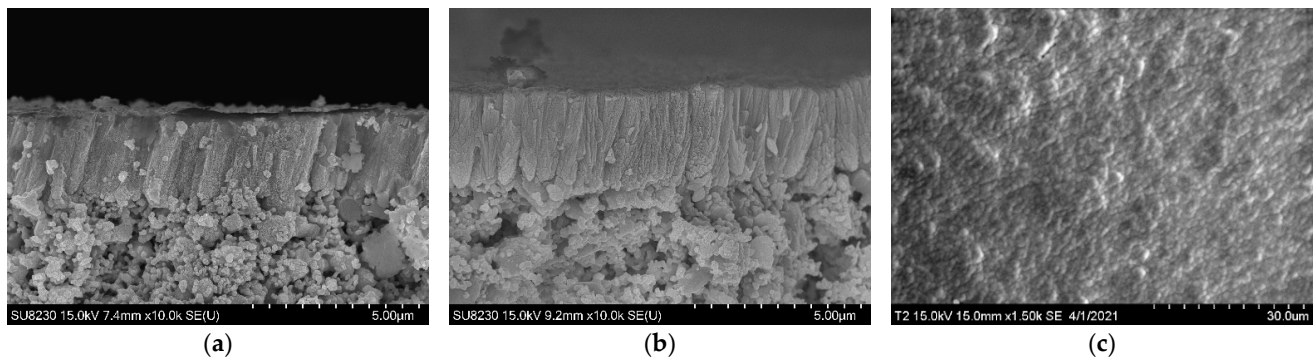


**Figure 8.** SEM micrographs presenting half-cell cross section, after electrolyte deposition (a), after densification by thermal treatment (b). The surface of the obtained half-cell is also presented (c).

A 3D microscopy is performed on the electrolyte after the annealing treatment at 1000 °C (Figure 9). The deposited layer follows the substrate topography. The height difference between the top and the bottom of the electrolyte surface remains near 3  $\mu\text{m}$ . Thus, even if the anode is perfectly covered, the resulting half-cells are not flat, as mentioned after SEM observations. Nevertheless, the electrolyte morphology allows it to play its insulator role between the electrodes and avoid contact between hydrogen and oxygen gases.

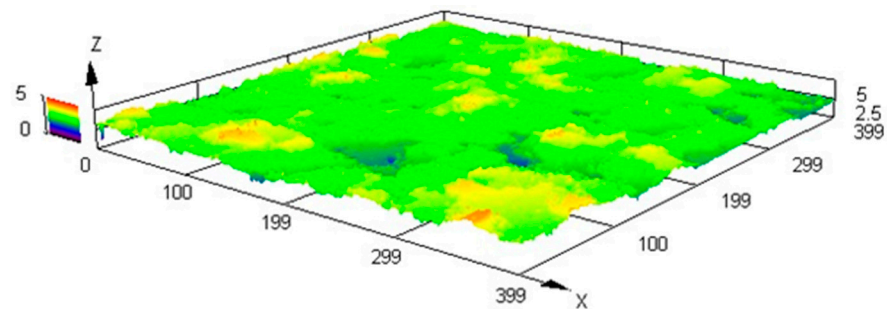


**Figure 9.** Three-dimensional microscopy of the deposited electrolyte (scale in  $\mu\text{m}$ ).

As presented earlier, different ratios of power applied to each target were tested to reach the right composition. Other parameters influence the aspect of the film. The first one is the substrate temperature during the deposition. As shown by Arab Pour Yazdi et al. [73], if the substrate is not heated during the deposition and without a heating treatment following the deposition, the film is unstable, and cracks are formed during the annealing treatment after the deposition stage. Another role of the temperature during the deposition is controlling the microstructure, along with the energy accumulated by the adatoms (which is partially correlated with the working pressure; the higher the pressure, the more collisions there will be between atoms, and the less energy they will have). In his study, Anders [74] proposes an extended structure zone diagram (SZD), which predicts the microstructure of the film as a function of these parameters. This diagram defines four zones with specific microstructures, and the parameters in this study were set to be in the columnar microstructure zone.

### 3.3. Study of the Cathode Part Deposited by Spray Coating

Finally, the cathode is deposited by spray coating on the electrolyte in order to obtain a complete cell. This step is followed by a thermal treatment at 800 °C under air. The cathode reaches a thickness of 30 µm. The results are presented in Figure 10a. The SEM picture shows an enlargement of the electrolyte area in a complete cell. It confirms the perfect adhesion between the anodic substrate, the electrolyte, and the cathode layers. Elemental analyses concerning the Ni (only in the anodic part) and Sr (only in the cathodic electrode) presences were also carried out on the electrolyte edges. The results, presented in Figure 10b, confirm the electrolyte thickness (>3 µm) and highlight the perfect interface both on the anode side and on the cathode side.

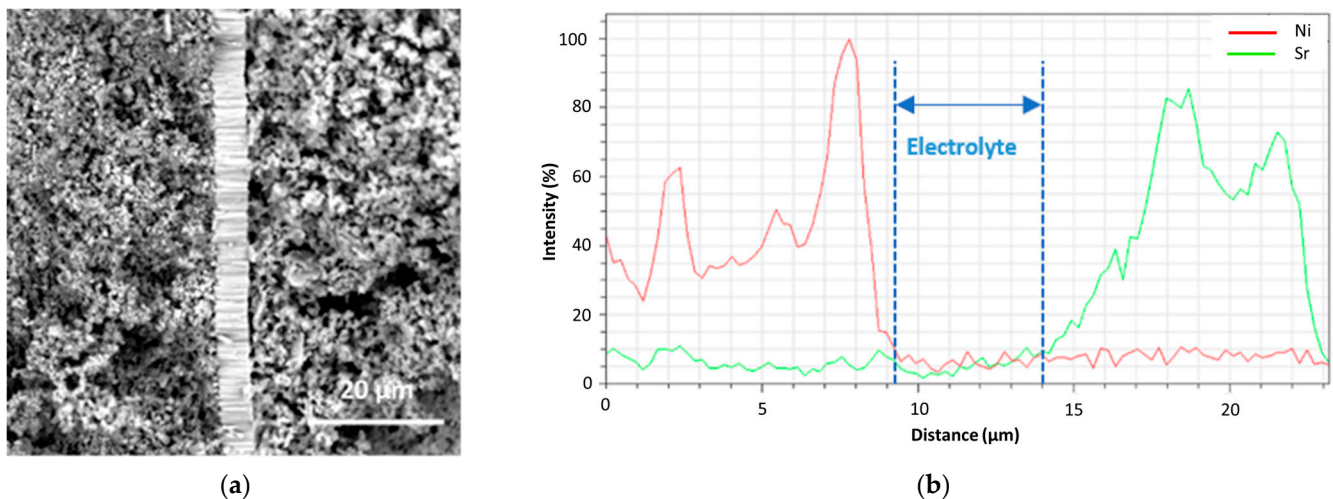


**Figure 10.** SEM micrographs (a) and elemental analysis (b) realized on a complete cell in an area closed to the electrolyte.

### 3.4. Impedance Measurement

The EIS spectra are presented in Figure 11a (Nyquist plot) and Figure 11b (Bode plot). The Nyquist plot consists of an inductive tail attributed to the electrical wires, followed by a skewed semi-circle. The ohmic resistance ( $R_{\Omega}$ ) taken at the intercept with the real part of the impedance at high frequencies is  $7.02 \Omega \text{ cm}^2$  and was stable for the duration of the measurements carried out at 525 °C (4 h). This value is significantly higher than other reported values for similar samples. For example, Bae et al. reported a  $R_{\Omega}$  of  $0.15 \Omega \text{ cm}^2$  for a Ni-BZY//BZY deposited by PLD (2 µm thick)// $\text{La}_{0.6}\text{Sr}_{0.4}\text{CoO}_{3-\delta}$  cell at 600 °C and Pergolesi et al. obtained a  $R_{\Omega}$  of  $1.85 \Omega \text{ cm}^2$  for a Ni-BZY//BZY deposited by PLD (4 µm thick)// $\text{La}_{0.6}\text{Sr}_{0.4}\text{C}_{0.2}\text{Fe}_{0.8}\text{O}_{3-\delta}$ - $\text{BaCe}_{0.9}\text{Yb}_{0.1}\text{O}_{3-\delta}$  cell at 600 °C [6,75]. However, the temperature has to be taken into account, since the diffusion is thermally activated, it is reasonable to suppose that the ohmic resistance of the BZY electrolyte deposited by reactive pulsed DC sputtering would have shown a lower resistance value at a higher temperature. In addition, the current collectors used in the homemade set-up were made of stainless steel, which probably led to an increase in the ohmic resistance due to the passivation layer.

Concerning the electrodes, the anode and cathode contributions cannot be separated due to the too-close characteristic time constant, as highlighted in the Bode plot. According to the shape of the Nyquist plot, the cathode process is not dominant, suggesting that the use of a composite material that presents protonic–electronic–oxygen ion conduction is beneficial for cell performance. The global polarization resistance is  $0.3 \Omega \cdot \text{cm}^2$ , similar to the lowest values reported in the literature [76]. Such a low value can be explained by the very low charge transfer resistances associated with the hydrogen oxidation reaction (HOR) and oxygen reduction reaction (ORR) due to the quality of the interfaces between the electrolyte and the electrodes.

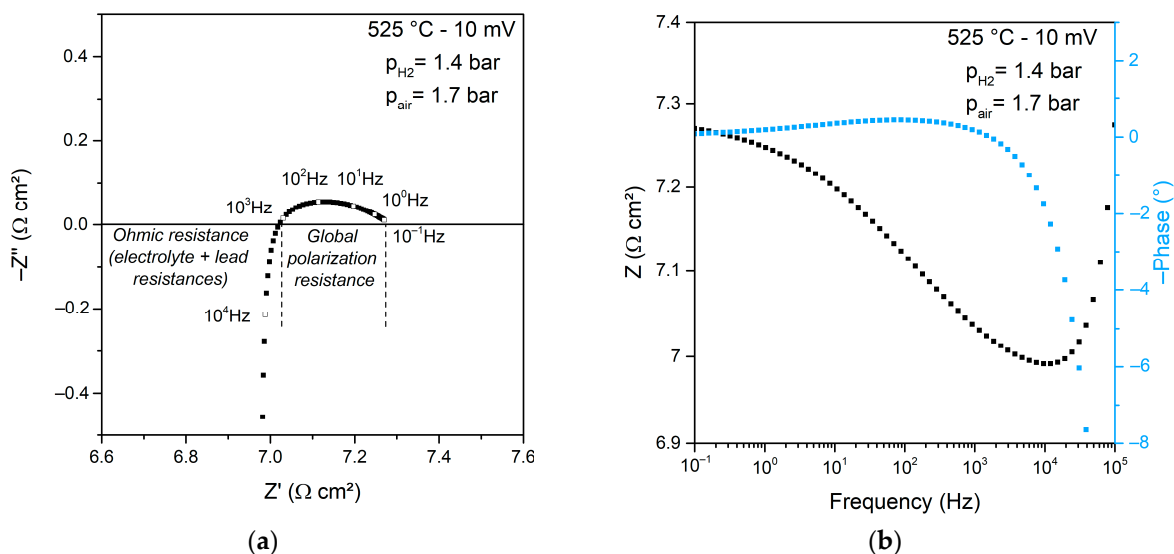


**Figure 11.** EIS spectra at OCV of a complete cell with an electrolyte deposited by reactive DC sputtering. (a) Nyquist plot and (b) Bode plot.

#### 4. Conclusions

In conclusion, this study serves as a compelling proof of concept, confirming the feasibility of this process sequence for realizing a complete ceramic fuel cell with a well-controlled electrolyte microstructure. This process sequence, meaning tape casting, DC magnetron sputtering, and spray coating, enables the production of a thin and dense electrolyte. Noteworthy advantages include excellent layer adhesion, the absence of delamination issues, and the ability to shape BZY, recognized for its refractory properties, at temperatures below 1350 °C. The EIS analysis reveals a higher ohmic resistance of  $7.02 \Omega \text{ cm}^2$ , possibly due to low temperature and stainless steel current collectors. However, a low overall polarization resistance of  $0.3 \Omega \text{ cm}^2$  was obtained, indicating efficient interfaces between electrolytes and electrodes thanks to the elaboration method.

**Author Contributions:** Conceptualization, V.L., M.F., L.C., P.B. and G.C.; methodology, V.L., M.F., E.A., L.C., P.B. and G.C.; validation, V.L., M.C. and E.A.; investigation, V.L., M.F. and M.C.; resources, L.C., P.B. and G.C.; writing—original draft preparation, V.L., M.F. and L.C.; writing—review and editing, V.L., M.C., E.A., P.B. and G.C.; visualization, V.L. and M.C.; supervision, P.B. and G.C.; project administration, L.C., P.B. and G.C.; funding acquisition, P.B. and G.C. All authors have read and agreed to the published version of the manuscript.

**Funding:** This work has been supported by the ISITE BFC (ANR-15-IDEX-0003). This work was also funded by the “France 2030” Plan (ANR-22-PEHY-0006) PROTEC Project, the Regional Council of Bourgogne Franche-Comté, the FEDER and the EIPHI Graduate School (ANR-17-EURE-0002).

**Data Availability Statement:** Dataset available on request from the authors.

**Acknowledgments:** The authors thank the Polytech Dijon Engineering College for the SEM and XRD facilities.

**Conflicts of Interest:** The authors declare no conflicts of interests.

#### Appendix A

Figure A1 is the diffractogram of the raw BZY powder. The perovskite phase of BZY is present and was attributed to ICDD file N°04-015-2511. A barium carbonate phase is also present and was attributed to ICDD file N°00-001-0506.

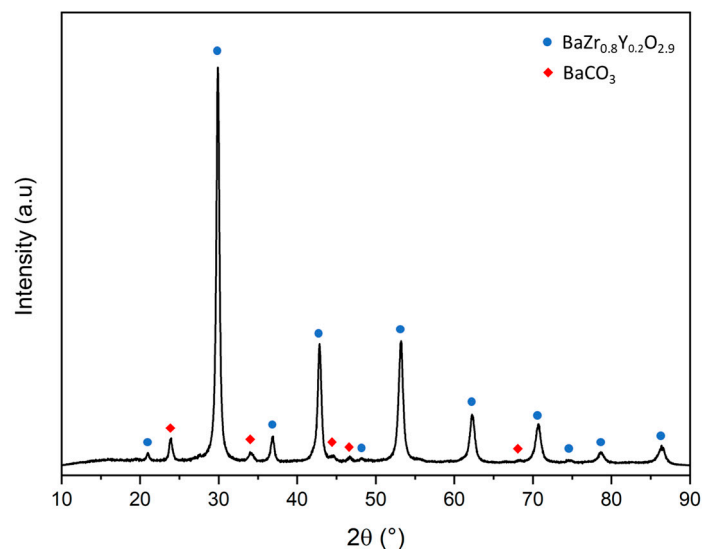


Figure A1. XRD pattern of BZY raw powder.

## References

- Han, D.; Shinoda, K.; Sato, S.; Majima, M.; Uda, T. Correlation between Electroconductive and Structural Properties of Proton Conductive Acceptor-Doped Barium Zirconate. *J. Mater. Chem. A* **2015**, *3*, 1243–1250. [\[CrossRef\]](#)
- Zhang, W.; Hu, Y.H. Progress in Proton-conducting Oxides as Electrolytes for Low-temperature Solid Oxide Fuel Cells: From Materials to Devices. *Energy Sci. Eng.* **2021**, *9*, 984–1011. [\[CrossRef\]](#)
- Xu, X.; Bi, L.; Zhao, X.S. Highly-Conductive Proton-Conducting Electrolyte Membranes with a Low Sintering Temperature for Solid Oxide Fuel Cells. *J. Membr. Sci.* **2018**, *558*, 17–25. [\[CrossRef\]](#)
- Choi, S.; Kucharczyk, C.J.; Liang, Y.; Zhang, X.; Takeuchi, I.; Ji, H.-I.; Haile, S.M. Exceptional Power Density and Stability at Intermediate Temperatures in Protonic Ceramic Fuel Cells. *Nat. Energy* **2018**, *3*, 202–210. [\[CrossRef\]](#)
- Bae, K.; Kim, D.H.; Choi, H.J.; Son, J.-W.; Shim, J.H. High-Performance Protonic Ceramic Fuel Cells with 1  $\mu\text{m}$  Thick Y:Ba(Ce,Zr)O<sub>3</sub> Electrolytes. *Adv. Energy Mater.* **2018**, *8*, 1801315. [\[CrossRef\]](#)
- Bae, K.; Jang, D.Y.; Choi, H.J.; Kim, D.; Hong, J.; Kim, B.-K.; Lee, J.-H.; Son, J.-W.; Shim, J.H. Demonstrating the Potential of Yttrium-Doped Barium Zirconate Electrolyte for High-Performance Fuel Cells. *Nat. Commun.* **2017**, *8*, 14553. [\[CrossRef\]](#) [\[PubMed\]](#)
- Khani, Z.; Taillades-Jacquin, M.; Taillades, G.; Marrony, M.; Jones, D.J.; Rozière, J. New Synthesis of Nanopowders of Proton Conducting Materials. A Route to Densified Proton Ceramics. *J. Solid State Chem.* **2009**, *182*, 790–798. [\[CrossRef\]](#)
- Kek, D.; Bonanos, N. Investigation of Hydrogen Oxidation Reaction on a Metal/Perovskite Proton Conductor Interface by Impedance Spectroscopy. *Vacuum* **2001**, *61*, 453–457. [\[CrossRef\]](#)
- Fabbri, E.; Oh, T.; Licoccia, S.; Traversa, E.; Wachsmann, E.D. Mixed Protonic/Electronic Conductor Cathodes for Intermediate Temperature SOFCs Based on Proton Conducting Electrolytes. *J. Electrochem. Soc.* **2009**, *156*, B38. [\[CrossRef\]](#)
- Nasani, N.; Dias, P.A.N.; Saraiva, J.A.; Fagg, D.P. Synthesis and Conductivity of Ba(Ce,Zr,Y)O<sub>3- $\delta$</sub>  Electrolytes for PCFCs by New Nitrate-Free Combustion Method. *Int. J. Hydrogen Energy* **2013**, *38*, 8461–8470. [\[CrossRef\]](#)
- Fabbri, E.; Pergolesi, D.; Traversa, E. Electrode Materials: A Challenge for the Exploitation of Protonic Solid Oxide Fuel Cells. *Sci. Technol. Adv. Mater.* **2010**, *11*, 044301. [\[CrossRef\]](#)
- Hossain, S.; Abdalla, A.M.; Jamain, S.N.B.; Zaini, J.H.; Azad, A.K. A Review on Proton Conducting Electrolytes for Clean Energy and Intermediate Temperature-Solid Oxide Fuel Cells. *Renew. Sustain. Energy Rev.* **2017**, *79*, 750–764. [\[CrossRef\]](#)
- Xu, X.; Bi, L. Proton-Conducting Electrolyte Materials. In *Intermediate Temperature Solid Oxide Fuel Cells*; Elsevier: Amsterdam, The Netherlands, 2020; pp. 81–111. ISBN 978-0-12-817445-6.
- Grimaud, A.; Bassat, J.M.; Mauvy, F.; Simon, P.; Canizares, A.; Rousseau, B.; Marrony, M.; Grenier, J.C. Transport Properties and In-Situ Raman Spectroscopy Study of BaCe<sub>0.9</sub>Y<sub>0.1</sub>O<sub>3- $\delta$</sub>  as a Function of Water Partial Pressures. *Solid State Ion.* **2011**, *191*, 24–31. [\[CrossRef\]](#)
- Bi, L.; Tao, Z.; Liu, C.; Sun, W.; Wang, H.; Liu, W. Fabrication and Characterization of Easily Sintered and Stable Anode-Supported Proton-Conducting Membranes. *J. Membr. Sci.* **2009**, *336*, 1–6. [\[CrossRef\]](#)
- Kreuer, K.D. Proton-Conducting Oxides. *Annu. Rev. Mater. Res.* **2003**, *33*, 333–359. [\[CrossRef\]](#)
- Rashid, N.L.R.M.; Samat, A.A.; Jais, A.A.; Somalu, M.R.; Muchtar, A.; Baharuddin, N.A.; Isahak, W.N.R.W. Review on Zirconate-Cerate-Based Electrolytes for Proton-Conducting Solid Oxide Fuel Cell. *Ceram. Int.* **2019**, *45*, 6605–6615. [\[CrossRef\]](#)
- Shi, Z.; Sun, W.; Wang, Z.; Qian, J.; Liu, W. Samarium and Yttrium Codoped BaCeO<sub>3</sub> Proton Conductor with Improved Sinterability and Higher Electrical Conductivity. *ACS Appl. Mater. Interfaces* **2014**, *6*, 5175–5182. [\[CrossRef\]](#)
- Akimune, Y.; Matsuo, K.; Higashiyama, H.; Honda, K.; Yamanaka, M.; Uchiyama, M.; Hatano, M. Nano-Ag Particles for Electrodes in a Yttria-Doped BaCeO<sub>3</sub> Protonic Conductor. *Solid State Ion.* **2007**, *178*, 575–579. [\[CrossRef\]](#)

20. Yahia, H.B.; Mauvy, F.; Grenier, J.C.  $\text{Ca}_{3-x}\text{La}_x\text{Co}_4\text{O}_{9+\delta}$  ( $X = 0, 0.3$ ): New Cobaltite Materials as Cathodes for Proton Conducting Solid Oxide Fuel Cell. *J. Solid State Chem.* **2010**, *183*, 527–531. [[CrossRef](#)]
21. Ryu, K.H.; Haile, S.M. Chemical Stability and Proton Conductivity of Doped  $\text{BaCeO}_3$ – $\text{BaZrO}_3$  Solid Solutions. *Solid State Ion.* **1999**, *125*, 355–367. [[CrossRef](#)]
22. Münch, W. Proton Diffusion in Perovskites: Comparison between  $\text{BaCeO}_3$ ,  $\text{BaZrO}_3$ ,  $\text{SrTiO}_3$ , and  $\text{CaTiO}_3$  Using Quantum Molecular Dynamics. *Solid State Ion.* **2000**, *136–137*, 183–189. [[CrossRef](#)]
23. Matsumoto, H.; Kawasaki, Y.; Ito, N.; Enoki, M.; Ishihara, T. Relation Between Electrical Conductivity and Chemical Stability of  $\text{BaCeO}_3$ -Based Proton Conductors with Different Trivalent Dopants. *Electrochem. Solid-State Lett.* **2007**, *10*, B77. [[CrossRef](#)]
24. Kim, D.; Lee, D.; Joo, J.H. Effect of Y-Doping on the Phase Relation and Electrical Properties of Fe-Doped  $\text{BaZrO}_3$ . *J. Eur. Ceram. Soc.* **2018**, *38*, 535–542. [[CrossRef](#)]
25. Fabbri, E.; Bi, L.; Pergolesi, D.; Traversa, E. Towards the Next Generation of Solid Oxide Fuel Cells Operating below 600 °C with Chemically Stable Proton-Conducting Electrolytes. *Adv. Mater.* **2012**, *24*, 195–208. [[CrossRef](#)] [[PubMed](#)]
26. Han, D.; Uda, T. The Best Composition of an Y-Doped  $\text{BaZrO}_3$  Electrolyte: Selection Criteria from Transport Properties, Microstructure, and Phase Behavior. *J. Mater. Chem. A* **2018**, *6*, 18571–18582. [[CrossRef](#)]
27. Dai, H.; Kou, H.; Wang, H.; Bi, L. Electrochemical Performance of Protonic Ceramic Fuel Cells with Stable  $\text{BaZrO}_3$ -Based Electrolyte: A Mini-Review. *Electrochem. Commun.* **2018**, *96*, 11–15. [[CrossRef](#)]
28. Kim, J.-H.; Kang, Y.-M.; Byun, M.-S.; Hwang, K.-T. Study on the Chemical Stability of Y-Doped  $\text{BaCeO}_{3-\delta}$  and  $\text{BaZrO}_{3-\delta}$  Films Deposited by Aerosol Deposition. *Thin Solid Films* **2011**, *520*, 1015–1021. [[CrossRef](#)]
29. Tong, J.; Clark, D.; Bernau, L.; Sanders, M.; O’Hayre, R. Solid-State Reactive Sintering Mechanism for Large-Grained Yttrium-Doped Barium Zirconate Proton Conducting Ceramics. *J. Mater. Chem.* **2010**, *20*, 6333. [[CrossRef](#)]
30. Fabbri, E.; Pergolesi, D.; Traversa, E. Materials Challenges toward Proton-Conducting Oxide Fuel Cells: A Critical Review. *Chem. Soc. Rev.* **2010**, *39*, 4355. [[CrossRef](#)]
31. Loureiro, F.J.A.; Nasani, N.; Reddy, G.S.; Munirathnam, N.R.; Fagg, D.P. A Review on Sintering Technology of Proton Conducting  $\text{BaCeO}_3$ – $\text{BaZrO}_3$  Perovskite Oxide Materials for Protonic Ceramic Fuel Cells. *J. Power Sources* **2019**, *438*, 226991. [[CrossRef](#)]
32. Katahira, K.; Kohchi, Y.; Shimura, T.; Iwahara, H. Protonic Conduction in Zr-Substituted  $\text{BaCeO}_3$ . *Solid State Ion.* **2000**, *138*, 91–98. [[CrossRef](#)]
33. Zhong, Z. Stability and Conductivity Study of the  $\text{BaCe}_{0.9-x}\text{Zr}_x\text{Y}_{0.1}\text{O}_{2.95}$  Systems. *Solid State Ion.* **2007**, *178*, 213–220. [[CrossRef](#)]
34. Pergolesi, D.; Fabbri, E.; D’Epifanio, A.; Di Bartolomeo, E.; Tebano, A.; Sanna, S.; Licocchia, S.; Balestrino, G.; Traversa, E. High Proton Conduction in Grain-Boundary-Free Yttrium-Doped Barium Zirconate Films Grown by Pulsed Laser Deposition. *Nat. Mater.* **2010**, *9*, 846–852. [[CrossRef](#)]
35. Zakaria, Z.; Awang Mat, Z.; Abu Hassan, S.H.; Boon Kar, Y. A Review of Solid Oxide Fuel Cell Component Fabrication Methods toward Lowering Temperature. *Int. J. Energy Res.* **2020**, *44*, 594–611. [[CrossRef](#)]
36. Lyu, Y.; Wang, F.; Wang, D.; Jin, Z. Alternative Preparation Methods of Thin Films for Solid Oxide Fuel Cells: Review. *Mater. Technol.* **2020**, *35*, 212–227. [[CrossRef](#)]
37. Nasani, N.; Ramasamy, D.; Brandão, A.D.; Yaremchenko, A.A.; Fagg, D.P. The Impact of Porosity,  $\text{pH}_2$  and  $\text{pH}_2\text{O}$  on the Polarisation Resistance of Ni– $\text{BaZr}_{0.85}\text{Y}_{0.15}\text{O}_{3-\delta}$  Cermet Anodes for Protonic Ceramic Fuel Cells (PCFCs). *Int. J. Hydrogen Energy* **2014**, *39*, 21231–21241. [[CrossRef](#)]
38. Liu, Y.; Shao, Z.; Mori, T.; Jiang, S.P. Development of Nickel Based Cermet Anode Materials in Solid Oxide Fuel Cells—Now and Future. *Mater. Rep. Energy* **2021**, *1*, 100003. [[CrossRef](#)]
39. Coors, W.G.; Manerbin, A. Characterization of Composite Cermet with 68 wt.% NiO and  $\text{BaCe}_{0.2}\text{Zr}_{0.6}\text{Y}_{0.2}\text{O}_{3-\delta}$ . *J. Membr. Sci.* **2011**, *376*, 50–55. [[CrossRef](#)]
40. Liu, Z.; Zhou, M.; Chen, M.; Cao, D.; Shao, J.; Liu, M.; Liu, J. A High-Performance Intermediate-to-Low Temperature Protonic Ceramic Fuel Cell with in-Situ Exsolved Nickel Nanoparticles in the Anode. *Ceram. Int.* **2020**, *46*, 19952–19959. [[CrossRef](#)]
41. Nasani, N.; Ramasamy, D.; Antunes, I.; Perez, J.; Fagg, D.P. Electrochemical Behaviour of Ni-BZO and Ni-BZY Cermet Anodes for Protonic Ceramic Fuel Cells (PCFCs)—A Comparative Study. *Electrochim. Acta* **2015**, *154*, 387–396. [[CrossRef](#)]
42. Wang, S.; Shen, J.; Zhu, Z.; Wang, Z.; Cao, Y.; Guan, X.; Wang, Y.; Wei, Z.; Chen, M. Further Optimization of Barium Cerate Properties via Co-Doping Strategy for Potential Application as Proton-Conducting Solid Oxide Fuel Cell Electrolyte. *J. Power Sources* **2018**, *387*, 24–32. [[CrossRef](#)]
43. Yang, L.; Zuo, C.; Wang, S.; Cheng, Z.; Liu, M. A Novel Composite Cathode for Low-Temperature SOFCs Based on Oxide Proton Conductors. *Adv. Mater.* **2008**, *20*, 3280–3283. [[CrossRef](#)]
44. Ricote, S.; Bonanos, N.; Rørvik, P.M.; Haavik, C. Microstructure and Performance of  $\text{La}_{0.58}\text{Sr}_{0.4}\text{Co}_{0.2}\text{Fe}_{0.8}\text{O}_{3-\delta}$  Cathodes Deposited on  $\text{BaCe}_{0.2}\text{Zr}_{0.7}\text{Y}_{0.1}\text{O}_{3-\delta}$  by Infiltration and Spray Pyrolysis. *J. Power Sources* **2012**, *209*, 172–179. [[CrossRef](#)]
45. Løken, A.; Ricote, S.; Wachowski, S. Thermal and Chemical Expansion in Proton Ceramic Electrolytes and Compatible Electrodes. *Crystals* **2018**, *8*, 365. [[CrossRef](#)]
46. Dailly, J.; Ancelin, M.; Marrony, M. Long Term Testing of BCZY-Based Protonic Ceramic Fuel Cell PCFC: Micro-Generation Profile and Reversible Production of Hydrogen and Electricity. *Solid State Ion.* **2017**, *306*, 69–75. [[CrossRef](#)]
47. Shi, H.; Yang, G.; Liu, Z.; Zhang, G.; Ran, R.; Shao, Z.; Zhou, W.; Jin, W. High Performance Tubular Solid Oxide Fuel Cells with BSCF Cathode. *Int. J. Hydrogen Energy* **2012**, *37*, 13022–13029. [[CrossRef](#)]

48. Toprak, M.S.; Darab, M.; Syvertsen, G.E.; Muhammed, M. Synthesis of Nanostructured BSCF by Oxalate Co-Precipitation—As Potential Cathode Material for Solid Oxide Fuels Cells. *Int. J. Hydrogen Energy* **2010**, *35*, 9448–9454. [[CrossRef](#)]
49. Ma, Y.; He, B.; Wang, J.; Cheng, M.; Zhong, X.; Huang, J. Porous/Dense Bilayer BaZr<sub>0.8</sub>Y<sub>0.2</sub>O<sub>3-δ</sub> Electrolyte Matrix Fabricated by Tape Casting Combined with Solid-State Reactive Sintering for Protonic Ceramic Fuel Cells. *Int. J. Hydrogen Energy* **2021**, *46*, 9918–9926. [[CrossRef](#)]
50. Liu, M.; Liu, Y. Multilayer Tape Casting of Large-Scale Anode-Supported Thin-Film Electrolyte Solid Oxide Fuel Cells. *Int. J. Hydrogen Energy* **2019**, *44*, 16976–16982. [[CrossRef](#)]
51. Yazdi, M.A.P.; Briois, P.; Billard, A. Influence of the Annealing Conditions on the Structure of BaCe<sub>1-x</sub>Y<sub>x</sub>O<sub>3-α</sub> Coatings Elaborated by DC Magnetron Sputtering at Room Temperature. *Mater. Chem. Phys.* **2009**, *117*, 178–182. [[CrossRef](#)]
52. Xiao, J.; Chen, L.; Yuan, H.; Ji, L.; Xiong, C.; Ma, J.; Zhu, X. Fabrication and Characterization of BaZr<sub>0.1</sub>Ce<sub>0.7</sub>Y<sub>0.2</sub>O<sub>3-δ</sub> Based Anode Supported Solid Oxide Fuel Cells by Tape Casting Combined with Spray Coating. *Mater. Lett.* **2017**, *189*, 192–195. [[CrossRef](#)]
53. Bi, L.; Traversa, E. Synthesis Strategies for Improving the Performance of Doped-BaZrO<sub>3</sub> Materials in Solid Oxide Fuel Cell Applications. *J. Mater. Res.* **2014**, *29*, 1–15. [[CrossRef](#)]
54. Han, D.; Jiang, L.; Zhong, P. Improving Phase Compatibility between Doped BaZrO<sub>3</sub> and NiO in Protonic Ceramic Cells via Tuning Composition and Dopant. *Int. J. Hydrogen Energy* **2021**, *46*, 8767–8777. [[CrossRef](#)]
55. Dayaghi, A.M.; Haugsrud, R.; Stange, M.; Larring, Y.; Strandbakke, R.; Norby, T. Increasing the Thermal Expansion of Proton Conducting Y-Doped BaZrO<sub>3</sub> by Sr and Ce Substitution. *Solid State Ion.* **2021**, *359*, 115534. [[CrossRef](#)]
56. Lescure, V.; Gelin, M.; François, M.; Arab Pour Yazdi, M.; Briois, P.; Demoisson, F.; Combemale, L.; Valton, S.; Caboche, G. X-Ray Micro-Computed Tomography: A Powerful Device to Analyze the 3D Microstructure of Anode-Electrolyte in BaZr<sub>0.8</sub>Y<sub>0.2</sub>O<sub>3</sub> Protonic Ceramic Electrochemical Cells and the Reduction Behavior. *Membranes* **2022**, *12*, 68. [[CrossRef](#)] [[PubMed](#)]
57. Gonçalves, M.D.; Maram, P.S.; Navrotsky, A.; Muccillo, R. Effect of Synthesis Atmosphere on the Proton Conductivity of Y-Doped Barium Zirconate Solid Electrolytes. *Ceram. Int.* **2016**, *42*, 13689–13696. [[CrossRef](#)]
58. Babilo, P.; Uda, T.; Haile, S.M. Processing of Yttrium-Doped Barium Zirconate for High Proton Conductivity. *J. Mater. Res.* **2007**, *22*, 1322–1330. [[CrossRef](#)]
59. Qin, G.; Bao, J.; Gao, J.; Ruan, F.; An, S.; Wang, Z.; Li, L. Enhanced Grain Boundary Conductivity of Gd and Sc Co-Doping BaZrO<sub>3</sub> Proton Conductor for Proton Ceramic Fuel Cell. *Chem. Eng. J.* **2023**, *466*, 143114. [[CrossRef](#)]
60. Fang, S.; Wang, S.; Brinkman, K.S.; Su, Q.; Wang, H.; Chen, F. Relationship between Fabrication Method and Chemical Stability of Ni-BaZr<sub>0.8</sub>Y<sub>0.2</sub>O<sub>3-δ</sub> Membrane. *J. Power Sources* **2015**, *278*, 614–622. [[CrossRef](#)]
61. Liu, Y.; Yang, L.; Liu, M.; Tang, Z.; Liu, M. Enhanced Sinterability of BaZr<sub>0.1</sub>Ce<sub>0.7</sub>Y<sub>0.1</sub>Yb<sub>0.1</sub>O<sub>3-δ</sub> by Addition of Nickel Oxide. *J. Power Sources* **2011**, *196*, 9980–9984. [[CrossRef](#)]
62. Arvanitidis, I.; Sichen, D.; Seetharaman, S. A Study of the Thermal Decomposition of BaCO<sub>3</sub>. *Metall. Mater. Trans. B* **1996**, *27*, 409–416. [[CrossRef](#)]
63. Choi, S.M.; Lee, J.-H.; Hong, J.; Kim, H.; Yoon, K.J.; Kim, B.-K.; Lee, J.-H. Effect of Sintering Atmosphere on Phase Stability, and Electrical Conductivity of Proton-Conducting Ba(Zr<sub>0.84</sub>Y<sub>0.15</sub>Cu<sub>0.01</sub>)O<sub>3-δ</sub>. *Int. J. Hydrogen Energy* **2014**, *39*, 7100–7108. [[CrossRef](#)]
64. François, M.; Carpanese, M.P.; Heintz, O.; Lescure, V.; Clematis, D.; Combemale, L.; Demoisson, F.; Caboche, G. Chemical Degradation of the La<sub>0.6</sub>Sr<sub>0.4</sub>Co<sub>0.2</sub>Fe<sub>0.8</sub>O<sub>3-δ</sub>/Ce<sub>0.8</sub>Sm<sub>0.2</sub>O<sub>2-δ</sub> Interface during Sintering and Cell Operation. *Energies* **2021**, *14*, 3674. [[CrossRef](#)]
65. Imashuku, S.; Uda, T.; Awakura, Y. Sintering Properties of Trivalent Cation-Doped Barium Zirconate at 1600 °C. *Electrochem. Solid-State Lett.* **2007**, *10*, B175. [[CrossRef](#)]
66. Kim, D.; Lee, T.K.; Han, S.; Jung, Y.; Lee, D.G.; Choi, M.; Lee, W. Advances and Challenges in Developing Protonic Ceramic Cells. *Mater. Today Energy* **2023**, *36*, 101365. [[CrossRef](#)]
67. Yamazaki, Y.; Hernandez-Sanchez, R.; Haile, S.M. Cation Non-Stoichiometry in Yttrium-Doped Barium Zirconate: Phase Behavior, Microstructure, and Proton Conductivity. *J. Mater. Chem.* **2010**, *20*, 8158. [[CrossRef](#)]
68. Panjan, P.; Drnovšek, A.; Gselman, P.; Čekada, M.; Panjan, M. Review of Growth Defects in Thin Films Prepared by PVD Techniques. *Coatings* **2020**, *10*, 447. [[CrossRef](#)]
69. Challali, F.; Mendil, D.; Touam, T.; Chauveau, T.; Bockelée, V.; Sanchez, A.G.; Chelouche, A.; Besland, M.-P. Effect of RF Sputtering Power and Vacuum Annealing on the Properties of AZO Thin Films Prepared from Ceramic Target in Confocal Configuration. *Mater. Sci. Semicond. Process.* **2020**, *118*, 105217. [[CrossRef](#)]
70. Zoppi, G.; Beattie, N.S.; Major, J.D.; Miles, R.W.; Forbes, I. Electrical, Morphological and Structural Properties of RF Magnetron Sputtered Mo Thin Films for Application in Thin Film Photovoltaic Solar Cells. *J. Mater. Sci.* **2011**, *46*, 4913–4921. [[CrossRef](#)]
71. Dong, X.; Su, Y.; Wu, Z.; Xu, X.; Xiang, Z.; Shi, Y.; Chen, W.; Dai, J.; Huang, Z.; Wang, T.; et al. Reactive Pulsed DC Magnetron Sputtering Deposition of Vanadium Oxide Thin Films: Role of Pulse Frequency on the Film Growth and Properties. *Appl. Surf. Sci.* **2021**, *562*, 150138. [[CrossRef](#)]
72. Lin, J.; Stinnett, T.C. Development of Thermal Barrier Coatings Using Reactive Pulsed Dc Magnetron Sputtering for Thermal Protection of Titanium Alloys. *Surf. Coat. Technol.* **2020**, *403*, 126377. [[CrossRef](#)]
73. Arab Pour Yazdi, M.; Briois, P.; Georges, S.; Costa, R.; Billard, A. Characterization of PCFC-Electrolytes Deposited by Reactive Magnetron Sputtering; Comparison with Ceramic Bulk Samples. *Fuel Cells* **2013**, *13*, 549–555. [[CrossRef](#)]
74. Anders, A. A Structure Zone Diagram Including Plasma-Based Deposition and Ion Etching. *Thin Solid Films* **2010**, *518*, 4087–4090. [[CrossRef](#)]

- 
75. Pergolesi, D.; Fabbri, E.; Traversa, E. Chemically Stable Anode-Supported Solid Oxide Fuel Cells Based on Y-Doped Barium Zirconate Thin Films Having Improved Performance. *Electrochem. Commun.* **2010**, *12*, 977–980. [[CrossRef](#)]
  76. Shao, Z.; Haile, S.M. A High-Performance Cathode for the next Generation of Solid-Oxide Fuel Cells. *Nature* **2004**, *431*, 170–173. [[CrossRef](#)] [[PubMed](#)]

**Disclaimer/Publisher’s Note:** The statements, opinions and data contained in all publications are solely those of the individual author(s) and contributor(s) and not of MDPI and/or the editor(s). MDPI and/or the editor(s) disclaim responsibility for any injury to people or property resulting from any ideas, methods, instructions or products referred to in the content.